IOP Publishing J. Phys.: Mater. 1 (2018) 015003 https://doi.org/10.1088/2515-7639/aac66e

JPhys Materials

OPEN ACCESS

RECEIVED
10 April 2018

REVISED
10 May 2018

ACCEPTED FOR PUBLICATION
21 May 2018

PUBLISHED
17 September 2018

Original content from this work may be used under the terms of the Creative Commons Attribution 3.0 licence.

Any further distribution of this work must maintain attribution to the author(s) and the title of the work, journal citation and DOI.

PAPER

Large scale graphene/h-BN heterostructures obtained by direct CVD growth of graphene using high-yield proximity-catalytic process

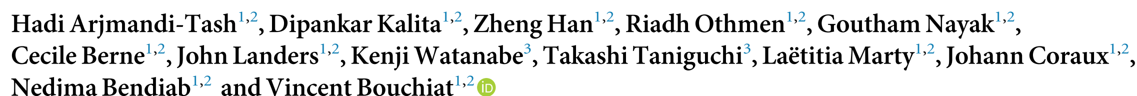

Hadi Arjmandi-Tash[1,2], **Dipankar Kalita**[1,2], **Zheng Han**[1,2], **Riadh Othmen**[1,2], **Goutham Nayak**[1,2], **Cecile Berne**[1,2], **John Landers**[1,2], **Kenji Watanabe**[3], **Takashi Taniguchi**[3], **Laëtitia Marty**[1,2], **Johann Coraux**[1,2], **Nedjma Bendiab**[1,2] **and Vincent Bouchiat**[1,2]

[1] Univ. Grenoble Alpes, Inst. Néel, F-38000 Grenoble, France
[2] CNRS, Inst. Néel, F-38000 Grenoble, France
[3] Advanced Materials Laboratory, National Institute for Materials Science, 1-1 Namiki, Tsukuba, 305-0044, Japan

E-mail: vincent.bouchiat@neel.cnrs.fr

Keywords: graphene, CVD, hexagonal boron nitride, copper, van der Waals heterostructure

Supplementary material for this article is available online

Abstract

We present a transfer-free process for the rapid growth of graphene on hexagonal boron nitride (h-BN) flakes via chemical vapor deposition. The growth of graphene on top of h-BN flakes is promoted by the adjacent copper catalyst. Full coverage of half-millimeter-sized h-BN crystals is demonstrated. The proximity of the copper catalyst ensures high-yield with a growth rate exceeding 2 μm min^{-1}, which is orders of magnitude above what was previously reported on h-BN and approaches the growth rate on copper. Optical and electron microscopies along with Raman mapping indicates a two-step growth mechanism, leading to the h-BN being first covered by discontinuous graphitic species prior to the formation of a continuous graphene layer. Electron transport measurements confirm the presence of well-crystallized and continuous graphene, which exhibits a charge carrier mobility that reaches 2.0×10^4 cm^2 V^{-1} s^{-1}. Direct comparison of the mobility with graphene/h-BN devices obtained by wet transfer confirms an enhanced charge neutrality for the *in situ* grown structures.

1. Introduction

Hexagonal boron nitride (h-BN) has been experimentally identified as an outstanding dielectric material for supporting graphene [1]. h-BN is a large bandgap semiconductor and its 2D lattice shares the same symmetry and almost identical lattice constant with graphene. Furthermore, it possesses a smooth and charge-neutral surface [2]. For all these reasons, h-BN buffer layers have shown to preserve the exceptional electronic properties of graphene [1], leading to long-range ballistic electron transport [3, 4] when graphene is fully encapsulated in between h-BN flakes. Moreover, the environmental 2D superpotential [5] induced on graphene by h-BN (giving rise to the so-called moiré pattern) has brought new physics within reach, such as the discovery of fractal quantum Hall effect characterized by an energy spectrum obeying the Hofstadter's butterfly pattern [6–8].

In most studies involving graphene embedded within two h-BN layers, the heterostructures were prepared by direct transfer of flakes using processes relying on physical adhesion via van der Waals interaction. This implies that graphene (exfoliated or chemically grown) is firstly isolated and then transferred onto h-BN host flakes. This manual critical step involves either micromanipulation of small flakes [1] or transfer of large area chemical vapor deposition (CVD)-grown graphene sheets based either on wet [5] or dry [9, 10] methods. Wrinkles, trapped air blisters, and polymeric residues are frequently found at the interfaces [11]. Besides, the alignment and transfer requires micromanipulation and thus presents low yield, which makes it incompatible with mass-production. However, alternative preparation techniques do exist, and have been reported as early as in 2000 [12, 13]. In these seminal works, graphene was grown by CVD onto a single layer of h-BN previously grown on a metal surface. Due to the extreme thinness of the h-BN buffer layer, the properties of graphene were not improved significantly [14]. The concept has recently been extended to less stringent conditions [15], and in

© 2018 The Author(s). Published by IOP Publishing Ltd

the absence of a metallic substrate, which is advantageous in the view of electronic devices [16–18]. Due to the absence of catalyst, graphene growth rate was found to be low (duration ranging from several tens of minutes [19] up to several hours [18, 20] to prepare a full layer), while the mechanisms driving the nucleation and growth are still ill-understood.

Indeed, the h-BN surface is inert towards the decomposition of hydrocarbons at the used growth temperatures. This issue can be circumvented by making the carbon precursor active prior to its adsorption on the surface, in plasma-enhanced CVD [20]. An elegant and easily implementable alternative was proposed by Kim *et al* [21], who demonstrated the lateral growth of graphene islands nucleating on a copper support and extending on top of single layer h-BN. Our work elaborates on this approach and establishes a high-yield lateral growth that can also occur on much thicker (up to 1 μm thick) and on larger (exceeding few tenths of a millimeter) h-BN crystals. Our technique relies on large exfoliated h-BN flakes with high crystalline quality. Note that the technique supports deposition of graphene on h-BN flakes of arbitrary thicknesses; particularly thick flakes (considerably thicker than few monolayers) bring about an enhanced electrical isolation of the graphene layer and facile transfer and handling of the heterostructures. We report a low residual charge carrier density of 4.5×10^{10} cm^{-2}, and an enhanced electronic mobility as high as 2.0×10^{4} cm^{2} V^{-1} s^{-1} at 80 K, close to the conductance saturation point. Finally, we provide a microscopic model describing the scattering of charge carriers in graphene on h-BN that is consistent with Raman spectroscopy and the charge carrier density-dependent electronic transport data.

2. Methods

We mechanically exfoliated h-BN flakes on copper foil (Alfa Aesar, CAS Number 7440-50-8, 25 μm thickness and 99.8% purity). We used two independent sources of h-BN material (i) high quality h-BN crystals grown by a high-pressure-high-temperature recrystalization method described in [22], achieving large flakes (above 100 μm in size) and (ii) commercially available h-BN flakes from Momentive with typical h-BN flake sizes of few tens of micrometers.The graphene is then grown by CVD using either classical (with continuous injection) [23] or pulsed injection [24] of methane at low-pressure. The latter technique is yielding to a continuous monolayer graphene, devoid of any multilayer patches. The thickness of the flakes after exfoliation on the copper ranged between 10 nm to few micrometer. In order to remove any glue residuals on the h-BN surfaces, prior to growth, the samples were annealed at 350 °C in the presence of hydrogen. (Figure 1(a), see methods for details). Then the temperature was increased up to 1020 °C for an annealing of ~ 1 h and then, the growth started. Continuous growth recipes is using CH_4 and H_2 gas (partial pressures, respectively of 2.8 μbar, and 0.1 mbar, argon used as dilution gas). For the pulsed injection recipe, the total growth duration was split into segments of duration 10 s with 55 s long interruption during which the CH_4 flow was off while hydrogen was kept constant. Depending on the total growth duration and on the flakes areas, partial or full coverage of h-BN flakes is achieved. To precisely study the kinetics and mechanism of the growth, the growth time is varied from 90 s up to 20 min, the longer time ensuring a full coverage of the surface even over hundreds-of-micrometer-scaled samples. For further analysis as well as for the purpose of device fabrication, graphene/h-BN heterostructures are then transferred onto oxidized silicon substrates using the usual Cu etching and wet transfer technique [23].

3. Results

3.1. Surface analysis of graphene/h-BN heterostructures

Optical (figure 1(a)), and scanning electron microscopy (SEM) (figures 1(d)–(f), and see figure S2 in the supplementary information (SI) available online at stacks.iop.org/JPMATER/1/015003/mmedia) images indicate that the surface of h-BN is free from apparent contaminant and appears homogeneous and surrounded by the copper surface without discontinuities. From atomic force microscopy (AFM) images (figure 1(c)) one can also distinguish Cu vicinal surface deformations around the h-BN flake indicative of a result of the reconstruction of the semi-liquid surface of the copper substrate during the high-temperature process. Such observation is important as it indicates that the Cu has the ability to wet the h-BN side walls of the crystal edges. The SEM picture shown in figure 1(b) further confirms the deformation of copper around the h-BN flake. The wetting of the crystal edges by Cu has a critical consequence as it suppresses the diffusion barrier at the border of h-BN flakes, for C species moving from the Cu surface to the otherwise protruding h-BN surface. Meanwhile the top surface of the h-BN flake keeps a very low roughness, as demonstrated by the high-resolution AFM micrograph (figure 1(g)) of the top layer taken from an area defined by the frame in figure 1(c). A histogram of the height distribution measured inside this window (figure 1(h)) reveals an rms roughness of ~4 Å, which is matching with the roughness of graphene on h-BN found in seminal works dealing with manual transferred

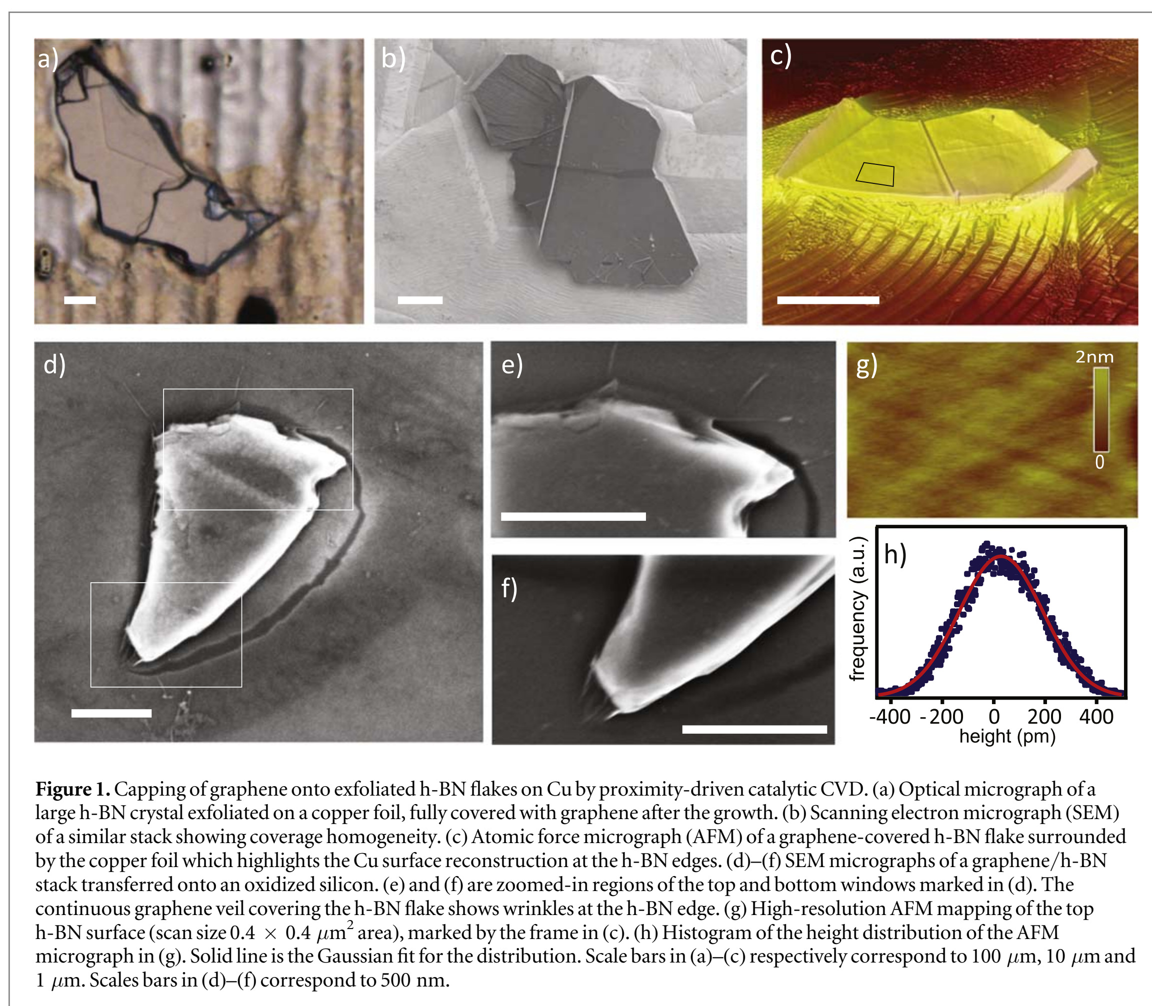

Figure 1. Capping of graphene onto exfoliated h-BN flakes on Cu by proximity-driven catalytic CVD. (a) Optical micrograph of a large h-BN crystal exfoliated on a copper foil, fully covered with graphene after the growth. (b) Scanning electron micrograph (SEM) of a similar stack showing coverage homogeneity. (c) Atomic force micrograph (AFM) of a graphene-covered h-BN flake surrounded by the copper foil which highlights the Cu surface reconstruction at the h-BN edges. (d)–(f) SEM micrographs of a graphene/h-BN stack transferred onto an oxidized silicon. (e) and (f) are zoomed-in regions of the top and bottom windows marked in (d). The continuous graphene veil covering the h-BN flake shows wrinkles at the h-BN edge. (g) High-resolution AFM mapping of the top h-BN surface (scan size $0.4 \times 0.4\ \mu m^2$ area), marked by the frame in (c). (h) Histogram of the height distribution of the AFM micrograph in (g). Solid line is the Gaussian fit for the distribution. Scale bars in (a)–(c) respectively correspond to 100 μm, 10 μm and 1 μm. Scales bars in (d)–(f) correspond to 500 nm.

stacks based on stamping technique [1]. Indeed, it appears that the surface quality of the h-BN is preserved during the high-temperature process and the deposited layer is intimately capping the top surface of h-BN.

To further assess the integrity of the graphene/h-BN, the flake together with the surrounding graphene is detached by wet etching of the Cu foil. SEM images of a graphene/h-BN heterostructure, after the whole stack has been transferred onto an oxidized silicon wafer, are shown in figures 1(d)–(f). It is worth noting that continuity of the graphene top veil is observed as the graphene grown on h-BN and outside the flakes are still connected, even-though the transferred graphene film is ruptured by some tearing caused by stress during the transfer (figure 1(d)). Ripples and bridges of locally suspended graphene are indeed observed (figures 1(e)–(f)) at some of the edges of the h-BN flake. This confirms the growth of graphene on h-BN flake and its continuity at the flake edges.

Figure 2 presents Raman characterization of a large ($\approx$60 000 μm^2) graphene-covered h-BN sample after being transferred onto oxidized silicon. Interestingly, typical Raman signatures [25] of a monolayer graphene are detectable everywhere on the sample, including at the positions where h-BN flakes are present. At these areas, the characteristic E_{2g} peak of h-BN is additionally detected (figure 2(a)) and the overall spectrum is absolutely similar to what is observed on CVD graphene transferred on h-BN flakes [26]. The overlapping of graphene and h-BN signatures unambiguously confirms the existence of graphene in contact with h-BN. Figure 2(b) shows the depth (y–z) mapping of the intensity of the E_{2g} mode of h-BN and of the 2D mode of graphene across a vertical line at the center of figure 2(d). Cutting profiles via the marked lines I (through h-BN) and O (outside h-BN) are also plotted in figure 2(c). Despite the focus broadening (caused by the beam waist), we can still observe a clear upshift of about 450 nm in the maximum intensity position of the 2D peak, as expected for graphene stepping up to the h-BN, further confirming the conformal top-coating of the h-BN with graphene. Figures 2(f) and (g) analyze the position of the G and 2D modes of graphene on the whole area. No remarkable discrepancy can be identified on h-BN and on copper foil and the frequencies are always in the expected range. Micro Raman scans clearly confirm, down to a 300 nm resolution, that graphene evenly covers large h-BN crystals, with no apparent limitation of coverage size (at least up to the millimeter square range which corresponds to the largest area of h-BN flakes produced by exfoliation). The fact that such large flakes are fully covered after 20 min growth implies a high speed of growth.

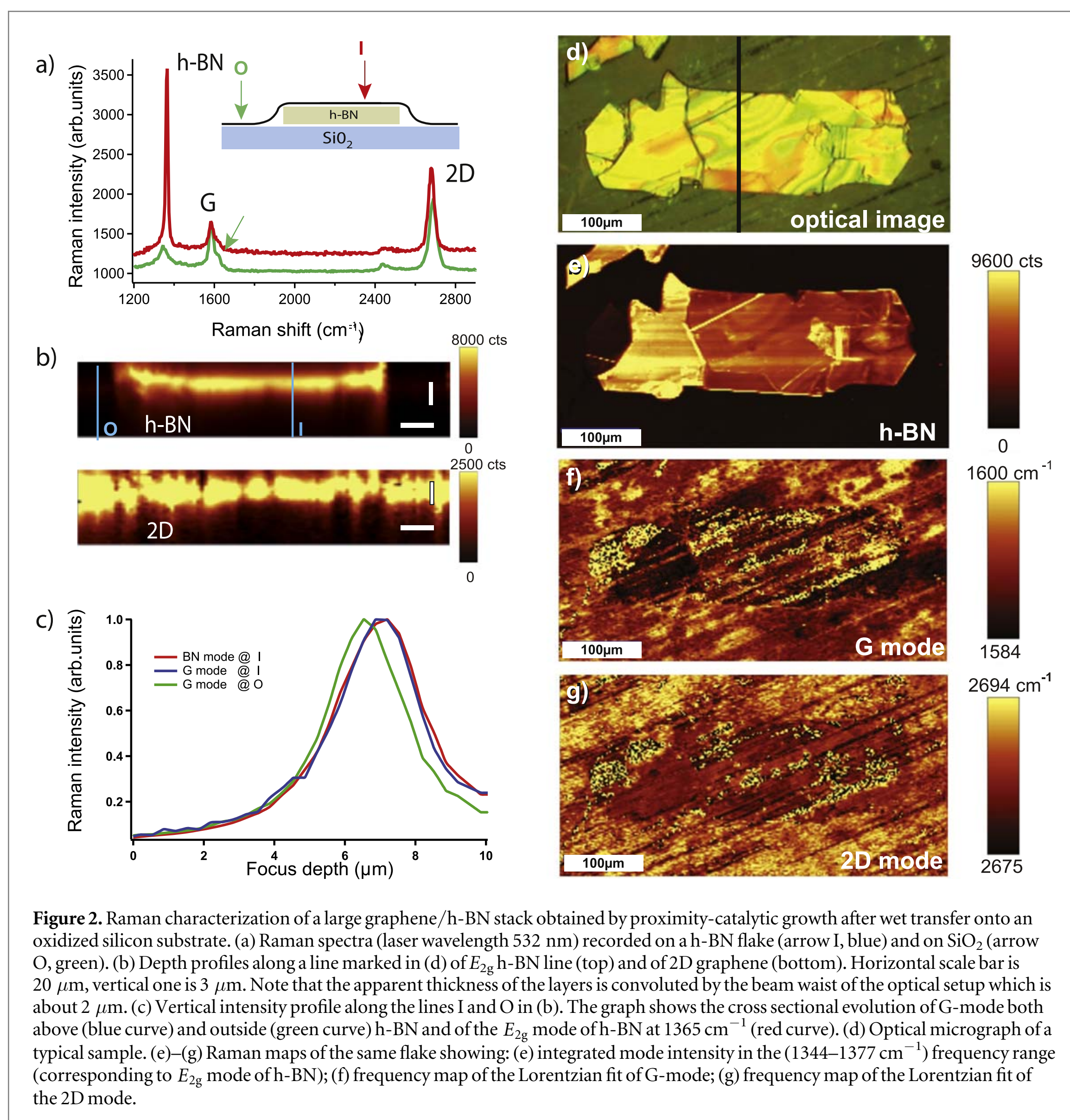

Figure 2. Raman characterization of a large graphene/h-BN stack obtained by proximity-catalytic growth after wet transfer onto an oxidized silicon substrate. (a) Raman spectra (laser wavelength 532 nm) recorded on a h-BN flake (arrow I, blue) and on SiO_2 (arrow O, green). (b) Depth profiles along a line marked in (d) of E_{2g} h-BN line (top) and of 2D graphene (bottom). Horizontal scale bar is 20 μm, vertical one is 3 μm. Note that the apparent thickness of the layers is convoluted by the beam waist of the optical setup which is about 2 μm. (c) Vertical intensity profile along the lines I and O in (b). The graph shows the cross sectional evolution of G-mode both above (blue curve) and outside (green curve) h-BN and of the E_{2g} mode of h-BN at 1365 cm^{-1} (red curve). (d) Optical micrograph of a typical sample. (e)–(g) Raman maps of the same flake showing: (e) integrated mode intensity in the (1344–1377 cm^{-1}) frequency range (corresponding to E_{2g} mode of h-BN); (f) frequency map of the Lorentzian fit of G-mode; (g) frequency map of the Lorentzian fit of the 2D mode.

We now turn towards the characterization of h-BN partially covered by graphene after an interrupted growth (i.e. samples for which methane injection was stopped before reaching full coverage). Typical results can be found in figures 3, 4(a) and in figure S2. Due to its conductive nature, graphene appears comparatively darker in SEM image compared to the bare Cu surface, which is oxidized immediately after growth due to the absence of the corrosion-protective graphene, and compared to the h-BN surface, which is insulating. This surface conductivity change generates a marked contrast in SEM micrographs which enables easy identification of the surface composition and allow estimation of the coverage ratio. Despite the non-catalytic activity of h-BN, it appears that the coverage ratio on Cu and on h-BN does not differ strongly at all these early stages of growth and that percolation is reached at similar times, after roughly 5 min of methane exposure (see bottom of figure 3, obtained at 240 s, just before full grain percolation is reached). To further investigate this, we have checked that the darker areas on the h-BN top surface are indeed covered with well-formed graphene.

This detailed Raman analysis of such partially covered h-BN is presented in figure 4. For the sake of clarity, we will note in the following by the letter A, the lighter zones (electron charging under the SEM) of h-BN and by letter B the darker (electron absorbing) zones on the same h-BN flakes. We find that the Raman spectra are strikingly different on zones A and B (figures 4(b)–(e)). While the B zone exhibits Raman spectra with both G and 2D modes characteristic of well-formed graphene, the zone A interestingly shows a broad G-peak and the absence of 2D peak which suggests the presence of defective graphitic carbon. Finally on the A zone, the G-mode is enhanced along the h-BN step edges (red arrow in figures 4(a) and (c)) which is probably associated with the accumulation of carbon species along defects.

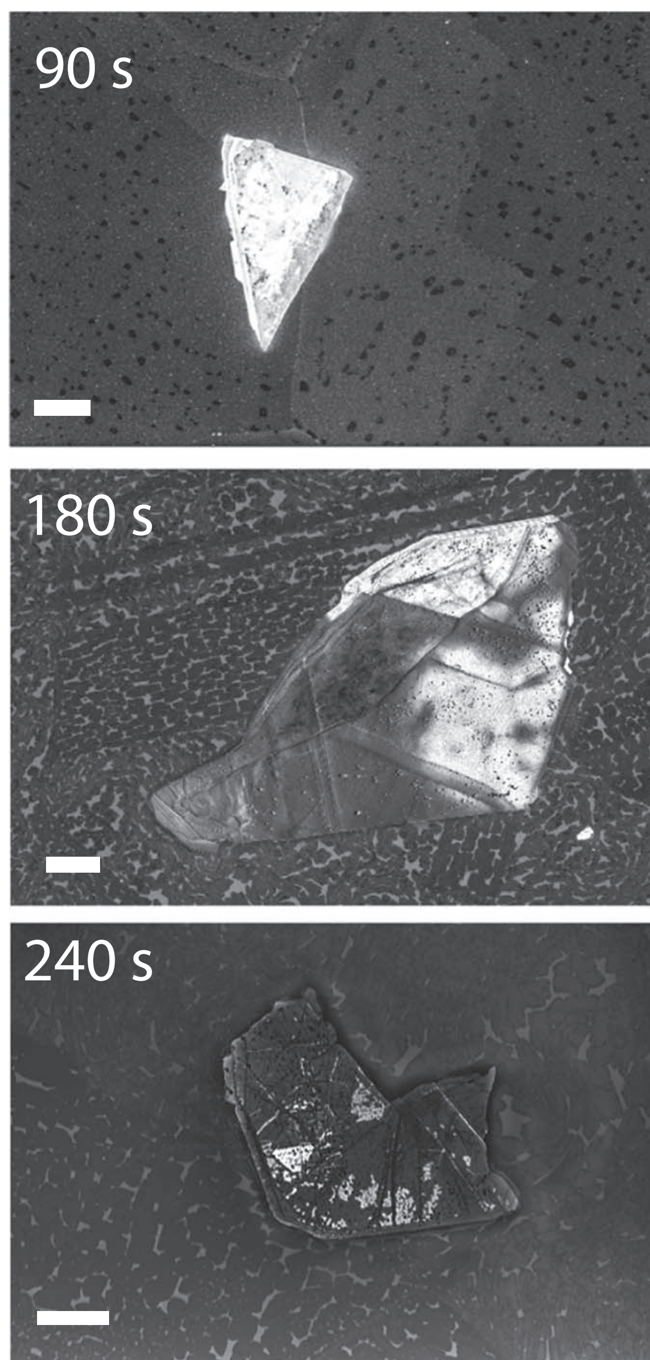

Figure 3. Growth kinetics: early stages of graphene coverage on h-BN and Cu surfaces. SEM micrographs of h-BN flakes on Cu imaged after respectively, 90 s, 180 s and 240 s growth time, showing partial coverage of graphene (darkest islands and zones). Note that the coverages of graphene on both Cu and h-BN surfaces are roughly equivalent in relative density, thus confirming the long lasting catalytic activity of Cu until full coverage of h-BN is achieved. Scale bars are 10 μm.

3.2. Mechanism of proximity-catalytic CVD growth of graphene onto h-BN flakes

From the observations of the previous section, one can propose a possible scenario for the growth mechanism. Firstly we found that after a 20 min growth, graphene covers inner areas of h-BN flakes at least 100 μm from crystal edges (as shown in figures 2(d)–(g), in which a half-millimeter flake is fully covered with graphene); secondly, when performing interrupted growth of 180 s duration, the complementary SEM and Raman analyses (figures 3 and S2) reveal that the edge of h-BN flakes are covered by graphene on a distance of ~4 to ~8 μm, which provides an estimation for the growth rate between 1.5 and 3 μm min^{-1}, a speed significantly exceeding the values recently reported in the case of direct-growth onto h-BN placed on the surface of silicon carbide [27] or involving deposition using molecular beam epitaxy [19, 28]. This distance is also matching the size of graphene grains found on the Cu foil just nearby (figures 3 and S2). In fact, the growth speed that we observe is in agreement with values reported for graphene growth on pure Cu [29], supporting a scenario involving a

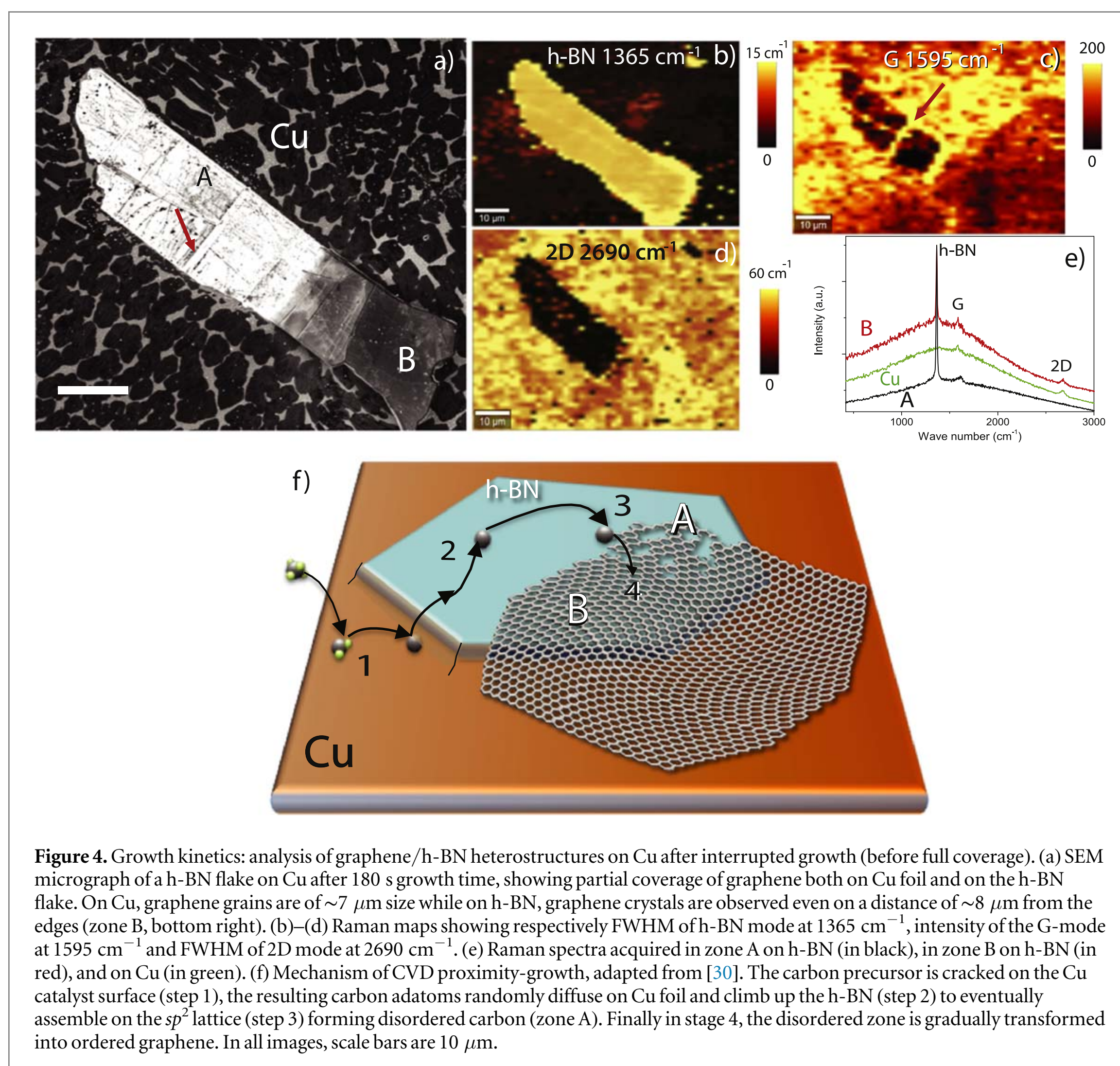

Figure 4. Growth kinetics: analysis of graphene/h-BN heterostructures on Cu after interrupted growth (before full coverage). (a) SEM micrograph of a h-BN flake on Cu after 180 s growth time, showing partial coverage of graphene both on Cu foil and on the h-BN flake. On Cu, graphene grains are of ~7 μm size while on h-BN, graphene crystals are observed even on a distance of ~8 μm from the edges (zone B, bottom right). (b)–(d) Raman maps showing respectively FWHM of h-BN mode at 1365 cm^{-1}, intensity of the G-mode at 1595 cm^{-1} and FWHM of 2D mode at 2690 cm^{-1}. (e) Raman spectra acquired in zone A on h-BN (in black), in zone B on h-BN (in red), and on Cu (in green). (f) Mechanism of CVD proximity-growth, adapted from [30]. The carbon precursor is cracked on the Cu catalyst surface (step 1), the resulting carbon adatoms randomly diffuse on Cu foil and climb up the h-BN (step 2) to eventually assemble on the sp^2 lattice (step 3) forming disordered carbon (zone A). Finally in stage 4, the disordered zone is gradually transformed into ordered graphene. In all images, scale bars are 10 μm.

proximity-growth with carbon adatoms, migrating from nearby Cu, as detailed in the following. The fact that Cu and h-BN are covered by graphene at a similar rate indicates that the catalytic cracking of the methane molecules is ongoing as long as graphene-free Cu regions exist, and that the resulting carbon atoms diffuse across the surface over several microns-distances.

h-BN is known to be a chemically-inert material well above 1000 °C [31]. Hence, no substantial decomposition of methane should occur on h-BN, and a methane molecule should rapidly desorb from h-BN with minimal chance of being activated/decomposed and involved in graphene growth. Several reports however revealed that the neighboring Cu, known to catalytically decompose methane (this is the essence of graphene CVD on bare Cu), generates the active C species for the growth of graphene away from the catalytic surface itself.

An alternative scenario invokes the presence of Cu in the gas phase (reasonably expected given the growth temperature) and/or on the reactor walls, that would activate methane before it reaches the surface [32, 33]. If at play, this effect should lead to the formation of graphene not only on h-BN, but also on graphene (leading to the formation of multilayer graphene), which we do not observe. Another possibility is that the h-BN surface is turned catalytically active by Cu in provenance from the surrounding Cu foil. While some clusters on the graphene/h-BN surface can occasionally be seen (figure S2) their spherical shape, charging properties under the SEM and similarities to what is usually observed during CVD in the absence of h-BN flakes indicate that they are more likely to be associated to silica particles. The presence of Cu wetting layer also is ruled out by our AFM measurements, showing a flat surface (figures 1(c), (g) and (h)). Finally we have not found any action of the Cu etching solution on the surface or interfaces of G/h-BN heterostuctures during the transfer on silicon substrates.

As we just pointed out, a uniform Raman 2D mode, characteristic of well-crystallized graphene, is only found after growth times of several minutes. For shorter growth times, the 2D mode is only observed close to the edges of h-BN (in the zone noted by letter B in figure 4(a)). The G-mode, on the contrary, appears almost uniformly distributed all over the h-BN surface, though, even for short growth times (figures 4(c) and (e)). These observations are characteristic of a progressive crystallization of graphene on h-BN. We tentatively interpret this

fact in the light of atomic scale processes at play having distinctive kinetics. We will mainly discuss three processes besides catalytic decomposition of methane by Cu: (i) diffusion of C atoms across the surface, (ii) attachment of C atoms at the graphene edges, and (iii) diffusion of C atoms, once they are attached at the graphene edges. Our observations suggest that the latter process is slower than the former ones. This also implies that defects are trapped during growth. The improved crystallinity of graphene upon increasing the growth time further suggests a finite mobility of trapped defects at the temperature employed during the growth; as time increases, the initially ill-crystallized graphene is progressively healed (e.g. by defect annihilation when two or few of them meet, or when they reach the edges of graphene). In addition, we expect defect healing to be aided by the feedstock of carbon atoms [34] continuously provided by the catalytic decomposition of methane by Cu.

At this point we can describe the main steps of the growth of graphene on h-BN as follows (figure 4(f)): methane is adsorbed at the Cu surface where it is readily decomposed into carbon adatoms. On the contrary, when landing on h-BN, methane is rapidly desorbed. As it is well known on Cu [35] and other low-C-solubility metals [36], the limiting step during graphene growth is the incorporation (attachment) of C at the graphene edges and the rearrangement into a 2D ordered crystal, while the diffusion of C adatoms across the surface is a comparatively very fast process. The latter implies that the nucleation is heterogeneous, occurring at defects of Cu, and rarely (with non-zero probability, though) on a h-BN surface, as it is the case on a graphene surface as well [37], where diffusion is considerably faster than on Cu. After the nucleation stage, graphene grows but leads to a disordered crystal (zone A) , finding in its surrounding a sufficient concentration of carbon adatoms to do so. Eventually, as the time during which the sample is at highest temperatures increases, graphenes quality is improved, yielding high-crystallinity graphene extending over macroscopic scales within several minutes. The mechanism we propose is supported by hundreds of measurements on a series of samples that have withstood different growth conditions (h-BN flake height, gas mixture composition). It is further supported by a set of specific measurements that have been interrupted at shorter times during graphene growth to generate partial coverage of graphene over h-BN to identify the shape and early organization of graphene growth on h-BN These 'time snapshots' samples have been analyzed by both SEM and Raman on h-BN flakes of different thicknesses.

As a conclusion for this section we have summarized our findings in the following:

- Overall SEM and Raman analyses support a basic principle of growth consistent with graphene flakes first nucleated on the copper catalyst, and further covering h-BN from its edges by the so-called 'proximity catalyst' effect.
- SEM analyses on interrupted growth time snapshots (figure 3) confirm that the kinetics of the growth is remarkably fast, actually faster than in previous reports of graphene growth on a non-catalytic surface. It is in fact as fast as on plain copper on the same sample.
- From the previous observations, further verified by numerous SEM measurements ($\gg$100) on h-BN of random thicknesses, taken from more than 20 growth batches using h-BN of different origins (commercial, provided by NIMS), we ascertained that the kinetics of surface coverage is independent from the h-BN thicknesses.
- The microscopy analyses (figures 1(b) and (c)) indicate that the h-BN flakes exfoliated on Cu looses their sharp side walls due to partial copper melting which wets the h-BN flake edges. In other words, the wetting angle of copper on the flake edge is high, preventing the Cu/h-BN border to act as a diffusion barrier.
- Spatial mappings of graphene's Raman modes (figure 4) unveil the presence of ill-crystallized carbon layer on h-BN in zones further away from the h-BN edges that are progressively replaced by crystalline graphene for longer growths.

3.3. Fabrication of electronic devices from the as-grown heterostructures

We now turn toward the use of transferred graphene/h-BN stacks for device fabrication and electron transport measurements. Oxygen plasma etching after transfer to SiO_2, is used to pattern graphene into a ribbon. The width of the resulting ribbon (figures 5(a) and (c)), is identical on top of h-BN and away from it, which would not be possible if graphene lied between h-BN and copper (before transferring) or between h-BN and SiO_2 (after transferring). Figure 5(c) also reveals the presence of another graphene region which shares a common edge with the h-BN flake indicating that it has been masked by the h-BN flake through the plasma process. This region is not detected in the optical (figure 5(a)) nor the SEM (figure 5(b)) images and thus is not lying on the surface. In-fact, the graphene at this region has been grown on the backside of h-BN or at the intermediate h-BN layers. We note that Raman visibility of the graphene through covering h-BN flakes is a known phenomenon [38].

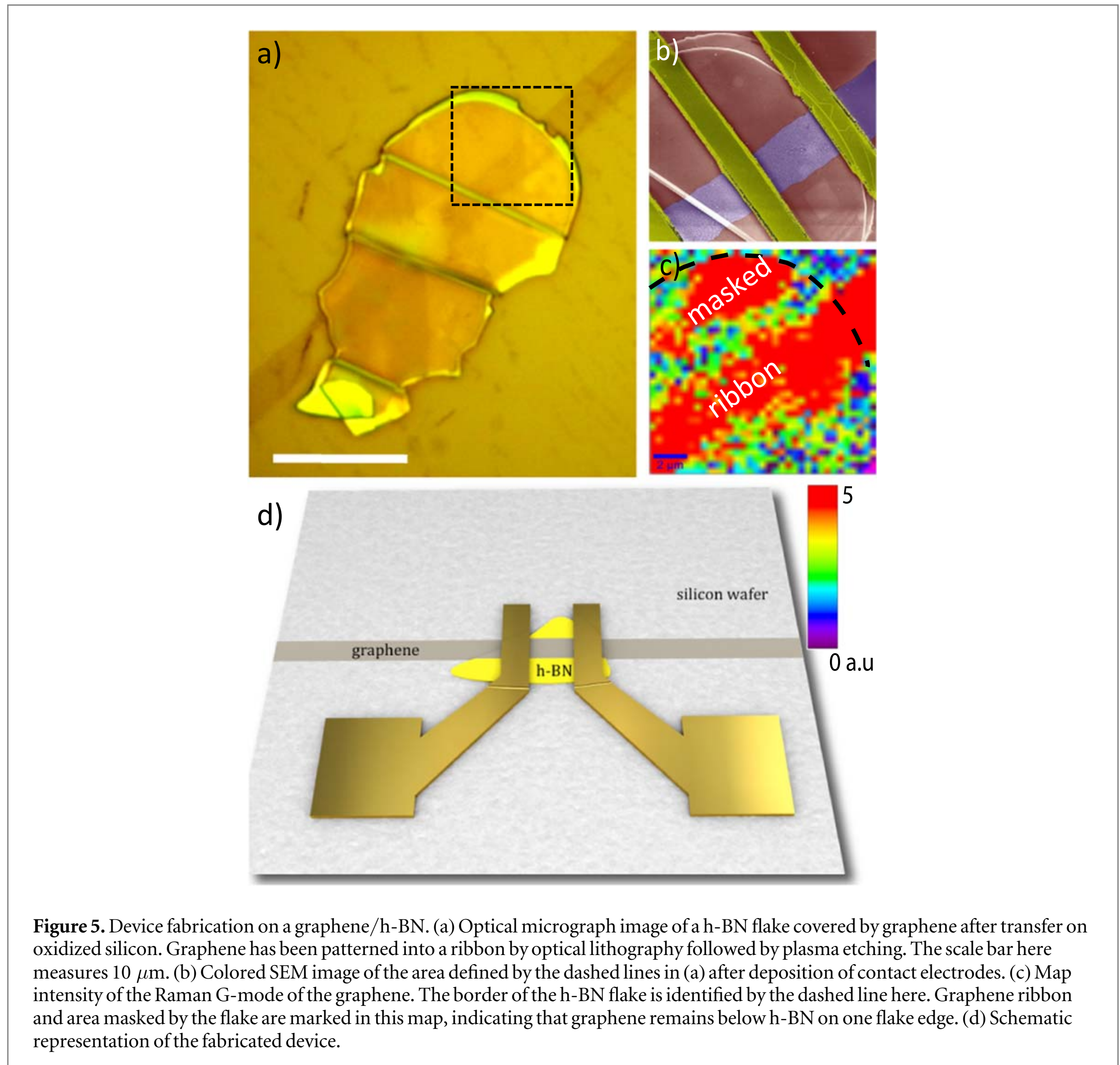

Figure 5. Device fabrication on a graphene/h-BN. (a) Optical micrograph image of a h-BN flake covered by graphene after transfer on oxidized silicon. Graphene has been patterned into a ribbon by optical lithography followed by plasma etching. The scale bar here measures 10 μm. (b) Colored SEM image of the area defined by the dashed lines in (a) after deposition of contact electrodes. (c) Map intensity of the Raman G-mode of the graphene. The border of the h-BN flake is identified by the dashed line here. Graphene ribbon and area masked by the flake are marked in this map, indicating that graphene remains below h-BN on one flake edge. (d) Schematic representation of the fabricated device.

3.4. Electron transport properties of graphene/h-BN devices

By depositing metal film electrodes on the graphene ribbon using electron beam lithography, we obtain a connected field-effect device. We compare the electronic properties of the sample obtained by the present technique (noted *DG*) with another graphene sample grown on Cu, but transferred onto an exfoliated h-BN (noted *TG*). All the electron transport measurements shown here were performed at 80 K and are summarized in figure 6. Comparisons at other temperatures (including room temperature can be found in figure 3 of the supplementary material).

Figure 6(a) shows the resistance as a function of the back-gate voltage of the two samples. The charge neutrality points for both samples are located close to zero voltage which is an indication of a clean graphene on a neutral h-BN substrate. The sample TG shows a sharper peak which is a signature of high mobility of charge carriers. These observations once more confirm the superior quality of graphene/h-BN compared to e.g. graphene/SiO_2. To quantitatively characterize the electronic performance of our samples, we now turn to a critical analysis of the factors limiting the electronic mobility in the system such as the sources of electron scattering. The field-effect curve shows a quite asymmetric pattern with a globally higher resistivity in the electron conduction regime than in the hole conduction regime. This can be attributed to doping from the metallic electrodes [39]. The asymmetry for the DG sample is even more pronounced; process residues on the sample could be a reason for that. The residual resistance (resistance at high gate voltages) is rather high for the TG sample, and it is even higher for the DG. This observation together with the presence of the resistivity fluctuations at high gate voltages indicates that both the samples and especially the DG one comprise a high population of short range crystalline defects. In CVD graphene such defects can be formed during growth, transfer or fabrication processes. Since both the samples have gone through similar fabrication steps, this observation in the DG sample can be attributed to the formation of defects during the growth.

There are few models that describe the scattering near the Dirac point in graphene [40, 41]. The existence of a D′ peak (arrow in figure 2(a)) in the Raman analysis suggests the existence of crystalline vacancies in our sample.

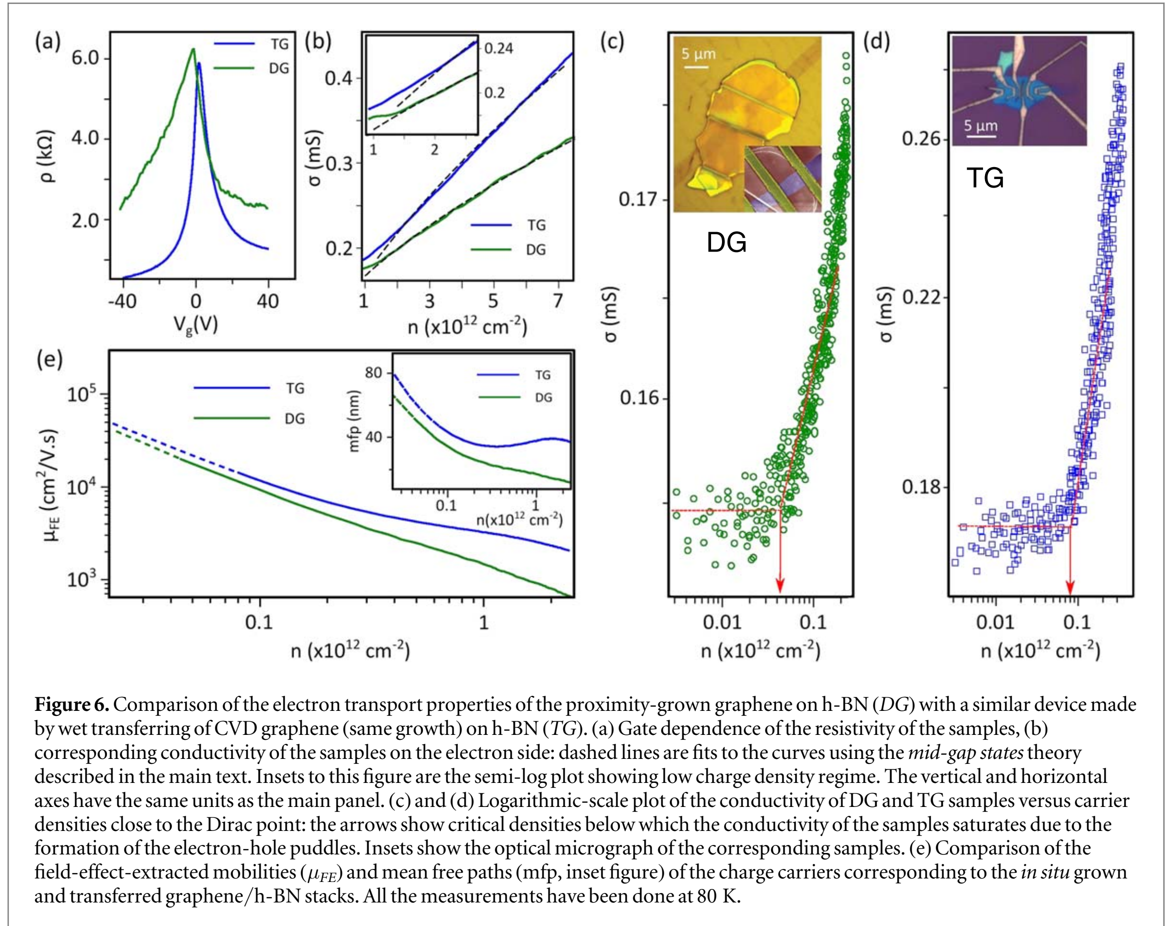

Figure 6. Comparison of the electron transport properties of the proximity-grown graphene on h-BN (*DG*) with a similar device made by wet transferring of CVD graphene (same growth) on h-BN (*TG*). (a) Gate dependence of the resistivity of the samples, (b) corresponding conductivity of the samples on the electron side: dashed lines are fits to the curves using the *mid-gap states* theory described in the main text. Insets to this figure are the semi-log plot showing low charge density regime. The vertical and horizontal axes have the same units as the main panel. (c) and (d) Logarithmic-scale plot of the conductivity of DG and TG samples versus carrier densities close to the Dirac point: the arrows show critical densities below which the conductivity of the samples saturates due to the formation of the electron-hole puddles. Insets show the optical micrograph of the corresponding samples. (e) Comparison of the field-effect-extracted mobilities (μ_{FE}) and mean free paths (mfp, inset figure) of the charge carriers corresponding to the *in situ* grown and transferred graphene/h-BN stacks. All the measurements have been done at 80 K.

Table 1. Defect parameters for different graphene samples.

	n_d (cm^{-2})	R_0 (Å)
Present work, TG	2.7×10^{12}	1.3
Present work, DG	4.0×10^{12}	1.5
Exfoliated graphene [42]	$< 10^{11}$	1.4

We hence use a model which considers scattering by such vacancies as *mid-gap states* [42]. In this model, strong disorder associated with the vacancies are modeled as deep potential wells [42, 43] and the conductivity is given by $\sigma = \frac{2e^2}{h}\frac{k_F^2}{\pi n_d}(\ln k_F R_0)^2$. Where k_F is the Fermi wave vector of graphene, n_d and R_0 refer to the density and characteristic size of the defects, respectively. Black dashed lines in figure 6(b) are the best fits to our experimental data, according to this model. Table 1 summarizes the parameters refined to achieve the best fits. For the sake of comparison, expected values for an exfoliated graphene [42] on typical substrates also are included in this table.

Clearly the size of the defects in our devices is in the atomic range and matches the predictions. However the population of such defects in our samples is at least one order of magnitude higher than the prediction for pristine graphene, hence appears as the main limitation to the mobility of charge carriers in both of the samples. Comparison of the data for TG and DG devices reveals that the indirect access to the catalyst during the growth of the DG sample leads to a slightly increased population of defects. We note that, unlike the TG, the DG sample was sandwiched and protected between a PMMA layer and h-BN flake during the transfer, thus the extra vacancies must have been formed during growth. Assuming that these vacancies are homogeneously spread all over the graphene and by considering the device geometries, the average spacing between the vacancies is estimated to be around 8 nm. We will see later (figure 6(e)) that at high carrier densities (when the role of the defects is important), the mean free path of the electrons in this sample falls below 10 nm which is very comparable to the spacing between the defects i.e. the transport of the charge carriers are affected by the formation of such vacancies.

The inset figure 6(b) focuses on the vicinity of the Dirac point. Here we see that by reducing the density of electrons, the model now fails to follow the experimental results. Around this area, the charged impurities close to the graphene sheet make a random network of 2D electron and hole puddles which affects the conductivity of the samples [44]. Interestingly, this transition happens at a higher carrier density for the TG sample. By plotting the low density regime in a logarithmic-scale (figures 6(c) and (d)), one can see by approaching the Dirac point that the conductivity of both of the samples reduces monotonically but saturates after a threshold density (n_{sat}, depicted by arrows there). The saturated conductivities for the samples ($\sigma_{satDG} \approx 1.0 \times \frac{4e^2}{h}$ and $\sigma_{satTG} \approx 1.1 \times \frac{4e^2}{h}$) are very close to the universal minimum conductivity predicted for graphene [42] which is reached below the threshold densities of $n_{satTG} \approx 8 \times 10^{10}\text{cm}^{-2}$ and $n_{satDG} \approx 4.5 \times 10^{10}\text{cm}^{-2}$ respectively. The ratio of the saturation density and the corresponding conductivity is proportional to the density of the charged impurities [41]: $n_{imp} \propto (\frac{n_{sat}}{\sigma_{sat}})$; this implies $n_{impDG}/n_{impTG} \approx 0.6$. This lower-than-one ratio clearly highlights the added-value of direct grown graphene (DG) compared to transferred graphene: it hosts a significantly lower density of charged impurities.

The thicknesses of the h-BN flake supporting the DG graphene sample is around 80 nm and knowing that the impurities located with a distance more than ≈10 nm from the graphene have a tiny effect on its conductivity [45], the estimated impurities in DG sample are either located on top of the graphene or are some impurities in the h-BN flake which might have migrated close to the surface during the growth.

Now we use the equation $\mu_{FE} = \sigma/en$ to calculate the electronic mobility of the samples. The results are plotted in figure 6(e). Atomic scale carbon vacancies can scatter charge carriers in a range that becomes comparable with their size (short range scatterers). As a result, the crystalline vacancies are effective scatterers only when charge carrier density is comparable to the defect density [40]. This is in contrast to charged defects which affect the transport of the charge carriers—via Coulomb interaction —even if they are far apart, including with much lower charge carrier concentration. The effect of the vacancies and charge impurities on the mobility have been analyzed theoretically. Indeed it is known that far from the Dirac point ($|V_g - V_D| \sim 100\text{V}$) the presence of the point defects may affect the mobility, reducing it by as much as one order of magnitude [42]. Comparison of the mobility of our samples also confirms the short range nature of the vacancy defects: close to the Dirac point, the difference between the field-effect mobility of the devices (for constant n) is negligible, while by increasing the charge density, the difference of the mobility corresponding to the samples with lower (TG) and higher (DG) vacancy defect concentration considerably increases.

The calculated field-effect mobilities are valid down to the onset of conductivity saturation [46]. The maximum mobility of TG at n_{satTG} is about 1.4×10^4 cm^2 V^{-1} s^{-1}, however the mobility of the DG continuously increases and approaches 2.0×10^4 cm^2 V^{-1} s^{-1} close to its saturation point. This mobility is one of the highest reported so far for graphene directly grown on h-BN in different techniques. From this curve, the corresponding mean free path (mfp) of the electrons can be calculated using the equation: $l = (h/2e)\mu\sqrt{n/\pi}$. The results are shown in the inset of figure 6(e). Like the mobility, early saturation of the conductivity for the DG, accounts for higher mean free paths for the DG.

4. Conclusions

In conclusion, our work introduces a new route to the high-yield chemical vapor deposition of graphene on thick non-catalyst materials (h-BN in our case) where a nearby catalyst indirectly promotes the growth on a refractory non-catalytic surface through collateral proximity effect . Two important consequences emerge from the presence of the catalyst in direct vicinity of the flakes: firstly, as the temperature during growth does not affect the surface quality of the h-BN flakes, most recipes developed for copper foils can be readily used for that growth, leading to full coverage of h-BN crystals with little to no change of parameters. Secondly, the presence of the catalyst ensures a high growth rate of strictly monolayer graphene on h-BN. We have shown that the approach is capable to deliver full coverage of graphene with kinetics similar to the graphene grown on the nearby catalyst and capping milimeter-sized exfoliated h-BN flakes in less than 20 min. Carbon species on h-BN after interrupted growth exist in two types (zone A and zone B in figure 4), each with specific signatures in Raman and under SEM. While areas covered by disordered carbon (zone A) dominates over areas covered by graphene (zone B) at very short growth times, the former zones tend to disappear at long growth times, leaving behind graphene exhibiting good mobility. The electron transport measurements in the regime of high charge carrier density showed that atomic-scaled vacancies hampers the electric transport of the produced graphene. The devices best perform close to the Dirac point, where the electron scattering is sensitive to lower amounts of charged impurities at the graphene/h-BN interface, keeping the formation of electron-hole puddles at voltages closer to global charge neutrality. In this regime, we obtained remarkably high carrier mobility which substantially exceed those found in manually transferred graphene/h-BN samples.

Acknowledgments

The authors are grateful for the help from the NanoFab team of Institut NEEL. HA-T. and JL acknowledges grant support from the Nanosciences Foundation of Grenoble. This work is partially supported by the French ANR contracts GRAPHMET, CLEANGRAPH and DIRACFORMAG, the EU contract NMP3-SL-2010-246073 from ERC, EU GRAPHENE Flagship and the Région Rhône-Alpes CIBLE program.

ORCID iDs

Vincent Bouchiat https://orcid.org/0000-0002-9818-8181

References

[1] Dean C R *et al* 2010 *Nat. Nanotechnol.* **5** 1–5
[2] Decker R, Wang Y, Brar V W, Regan W, Tsai H-Z, Wu Q, Gannett W, Zettl A and Crommie M F 2011 *Nano Lett.* **11** 2291–5
[3] Mayorov A S *et al* 2011 *Nano Lett.* **11** 2396–9
[4] Wang L *et al* 2013 *Science* **342** 614–7
[5] Xue J, Sanchez-Yamagishi J, Bulmash D, Jacquod P, Deshpande A, Watanabe K, Taniguchi T, Jarillo-Herrero P and LeRoy B J 2011 *Nat. Mater.* **10** 282–5
[6] Yankowitz M, Xue J, Cormode D, Sanchez-Yamagishi J D, Watanabe K, Taniguchi T, Jarillo-Herrero P, Jacquod P and LeRoy B J 2012 Emergence of superlattice Dirac points in graphene on hexagonal boron nitride *Nat. Phys.* **8** 382–6
[7] Dean C R *et al* 2013 *Nature* **497** 598–602
[8] Hunt B *et al* 2013 *Science* **340** 1427–30
[9] Petrone N, Dean C R, Meric I, van der Zande A M, Huang P Y, Wang L, Muller D, Shepard K L and Hone J 2012 *Nano Lett.* **12** 2751–6
[10] Banszerus L, Schmitz M, Engels S, Dauber J, Oellers M, Haupt F, Watanabe K, Taniguchi T, Beschoten B and Stampfer C 2015 *Sci. Adv.* **1** e1500222
[11] Haigh S J, Gholinia A, Jalil R, Romani S, Britnell L, Elias D C, Novoselov K S, Ponomarenko L A, Geim A K and Gorbachev R 2012 *Nat. Mater.* **11** 764–7
[12] Oshima C, Itoh A, Rokuta E, Tanaka T, Yamashita K and Sakurai T 2000 *Solid State Commun.* **116** 37–40
[13] Kawasaki T, Ichimura T, Kishimito H, Akbar A A, Ogawa T and Oshima C 2002 *Surf. Rev. Lett.* **9** 1459–64
[14] Roth S, Matsui F, Greber T and Osterwalder J 2013 *Nano Lett.* **13** 2668–75
[15] Wang M *et al* 2013 *Adv. Mater.* **25** 2746–52
[16] Son M, Lim H, Hong M and Choi H C 2011 *Nanoscale* **3** 3089–93
[17] Ding X, Ding G, Xie X, Huang F and Jiang M 2011 *Carbon* **49** 2522–5
[18] Tang S, Ding G, Xie X, Chen J, Wang C, Ding X, Huang F, Lu W and Jiang M 2012 *Carbon* **50** 329–31
[19] Garcia J M *et al* 2012 *Solid State Commun.* **152** 975–8
[20] Yang W *et al* 2013 *Nat. Mater.* **12** 792–7
[21] Kim S M, Hsu A, Araujo P T, Lee Y-H, Palacios T, Dresselhaus M, Idrobo J-C, Kim K K and Kong J 2013 *Nano Lett.* **13** 933–41
[22] Taniguchi T and Watanabe K 2007 *J. Cryst. Growth* **303** 525–9
[23] Li X *et al* 2009 *Science* **324** 1312–4
[24] Han Z *et al* 2014 *Adv. Funct. Mater.* **24** 964–70
[25] Ferrari A C 2007 *Solid State Commun.* **143** 47–57
[26] Souibgui M, Ajlani H, Cavanna A, Oueslati M, Meftah A and Madouri A 2017 *Superlattices Microstruct.* **112** 394–403
[27] Mishra N, Miseikis V, Convertino D, Gemmi M, Piazza V and Coletti C 2016 *Carbon* **96** 497–502
[28] Garcia J M *et al* 2013 Graphene growth on h-BN by Van der Waals MBE *March Meeting 2013* vol 2 (American Physical Society)
[29] Wu T *et al* 2016 *Nat. Mater.* **15** 43–7
[30] Kim S M, Hsu A, Araujo P T, Lee Y-H, Palacios T, Dresselhaus M, Idrobo J-C, Kim K K and Kong J 2013 *Nano Lett.* **13** 933–41
[31] Kostoglou N, Polychronopoulou K and Rebholz C 2015 *Vacuum* **112** 42–5
[32] Kim H, Song I, Park C, Son M, Hong M, Kim Y, Kim J S, Shin H-J, Baik J and Choi H C 2013 *ACS Nano* **7** 6575–82
[33] Teng P-Y, Lu C-C, Akiyama-Hasegawa K, Lin Y-C, Yeh C-H, Suenaga K and Chiu P-W 2012 Remote catalyzation for direct formation of graphene layers on oxides *Nano Lett.* **12** 1379–84
[34] Song B, Schneider G F, Xu Q, Pandraud G, Dekker C and Zandbergen H 2011 *Nano Lett.* **11** 2247–50
[35] Kim H, Mattevi C, Calvo M R, Oberg J C, Artiglia L, Agnoli S, Hirjibehedin C F, Chhowalla M and Saiz E 2012 *ACS Nano* **6** 3614–23
[36] Coraux J, N'Diaye A T, Engler M, Busse C, Wall D, Buckanie N, zu Heringdorf F-J M, van Gastel R, Poelsema B and Michely T 2009 *New J. Phys.* **11** 023006
[37] Lehtinen P O, Foster A S, Ayuela A, Krasheninnikov A, Nordlund K and Nieminen R M 2003 *Phys. Rev. Lett.* **91** 017202
[38] Wang L, Chen Z, Dean C R, Taniguchi T, Watanabe K, Brus L E and Hone J 2012 *ACS Nano* **6** 9314–9
[39] Wu Y, Perebeinos V, Lin Y-M, Low T, Xia F and Avouris P 2012 *Nano Lett.* **12** 1417–23
[40] Hwang E, Adam S and Sarma S 2007 *Phys. Rev. Lett.* **98** 186806
[41] Adam S, Hwang E H, Galitski V M and Das Sarma S 2007 *Proc. Natl Acad. Sci.* **104** 18392–7
[42] Stauber T, Peres N and Guinea F 2007 *Phys. Rev.* B **76** 205423
[43] Hentschel M and Guinea F 2007 *Phys. Rev.* B **76** 115407
[44] Martin J, Akerman N, Ulbricht G, Lohmann T, Smet J H, Von Klitzing K and Yacoby A 2007 *Nat. Phys.* **4** 144–8
[45] Chen J-H, Cullen W, Jang C, Fuhrer M and Williams E 2009 *Phys. Rev. Lett.* **102** 236805
[46] Du X, Skachko I, Barker A and Andrei E Y 2008 *Nat. Nanotechnol.* **3** 491–5